https://doi.org/10.15407/ujpe71.9.763

R.YA. LESHKO,[1] O.V. LESHKO,[1] I.V. BILYNSKYI,[1,2] D.S. KARPYN[1]

[1] Department of Physics and Information Systems,
Drohobych Ivan Franko State Pedagogical University
(3, Stryiska Str., Drohobych 82100, Ukraine)

[2] Department of Physics, Kryvyi Rih State Pedagogical University
(54, Universytetska Str., Kryvyi Rih 50086, Ukraine)

EXCITON STATES IN SPHERICAL NON-CONCENTRIC CORE–SHELL QUANTUM DOTS

The electronic and excitonic structure of non-concentric CdSe/CdS core-shell spherical quantum dots is investigated theoretically, with the core rigidly displaced from the shell center. Hole states are computed within the four-band Luttinger–Kohn model expanded in a plane-wave basis, with the displaced-core confining potential treated exactly, and exciton states are obtained by configuration interaction including the direct electron-hole Coulomb attraction and the short-range exchange interaction. The displacement reduces the confining symmetry from spherical to axial and lifts the degeneracy of the band-edge hole multiplet, yielding a fine-structure splitting that increases monotonically with the core offset. The same mechanism reshapes the exciton spectrum: the ground-state transition undergoes a blueshift as the core approaches the shell boundary, while the exchange-induced dark–bright splitting grows steadily with displacement. The calculated absorption edge is in quantitative agreement with the experimentally measured value. This agreement is obtained only when excitonic effects are included, with the electron-hole Coulomb attraction supplying the redshift required to reconcile theory and experiment. The results identify the core displacement as an effective structural degree of freedom for tuning both the emission energy and the exciton fine structure of colloidal core-shell nanocrystals.

K e y w o r d s: core–shell quantum dot, non-concentric nanostructure, CdSe/CdS, exciton fine structure, dark-bright splitting, electron-hole exchange interaction, Luttinger–Kohn Hamiltonian, plane-wave expansion method.

1. Introduction

Semiconductor quantum dots (QDs) have become an integral component of modern nanophotonics and optoelectronics due to their unique, size-tunable optical and electronic properties. Among the variety of nanoscale systems, core-shell heterostructures occupy a special place. The ability to select core and shell materials with different band gaps and band alignments allows such QDs to effectively control the spatial localization of charge carriers and the probability of radiative transitions [1–4]. This makes them critically important for the development of advanced optoelectronic devices. In particular, the core-shell architecture is key to the design of highly efficient luminescent solar concentrators [1, 5, 6], as it enables a significant Stokes shift [6], thereby minimizing self-absorption losses. Furthermore, the controlled spatial separation of the electron-hole pair and the consequent suppression of non-radiative Auger recombination have paved the way for the creation of highly stable, so-called non-blinking light-emitting diodes and reliable single-photon sources [7].

Among the various fabrication techniques developed to date, colloidal synthesis remains one of the most versatile and widely adopted methods for producing core-shell QDs. This chemical approach, particularly in the organic phase, has been successfully employed to realize the aforementioned non-blinking nanostructures [8, 9]. For instance, by pre-

C i t a t i o n: Leshko R.Ya., Leshko O.V., Bilynskyi I.V., Karpyn D.S. Exciton states in spherical non-concentric core–shell quantum dots. *Ukr. J. Phys.* **71**, No. 9, 763 (2026). https://doi.org/10.15407/ujpe71.9.763.

cisely controlling the deposition of CdS shell layers onto pre-grown CdSe cores, researchers can systematically tune the overall dimensions of the resulting samples [9]. Because these QDs are grown in colloidal solutions, the minimization of surface tension typically drives them to adopt a quasi-spherical geometry. However, despite the common theoretical assumption of perfect spatial symmetry, actual colloidal synthesis does not guarantee concentricity of the core and shell. In real experimental samples, factors such as nonuniform shell growth rates, localized lattice mismatch strains, or kinetic fluctuations during the chemical deposition process frequently cause the core to be displaced from the geometric center of the shell. Consequently, the actual morphology of these synthesized nanoparticles often corresponds to a nonconcentric spherical core-shell QD (NCSCSQD) [10].

To date, a substantial body of theoretical work has been dedicated to studying NCSCSQDs. Various theoretical approaches, including the plane wave expansion method and other numerical techniques, have been successfully applied to model these systems [10–14]. These studies have extensively explored the energy spectra of charge carriers under the influence of external electric and magnetic fields, and have investigated the electron-hole exchange interaction [15]. However, a major limitation of these previous investigations is their simplified treatment of the hole states. They predominantly relied on a simple single-band effective mass model, thereby completely neglecting the complex structure of the valence band and the inherent mixing between heavy and light hole states. This crucial theoretical gap can be closed by utilizing the Luttinger Hamiltonian [16–18], specifically within the Baldereschi–Lipari spherical approximation [19], which accurately captures the complex valence band dynamics.

Furthermore, although earlier works have calculated various optical parameters and transition probabilities in NCSCSQDs [12], they largely overlooked excitonic effects. In strongly confined nanoscale systems, the Coulomb interaction between the electron and the hole is highly pronounced. Neglecting exciton formation results in an incomplete description of the optical response and leads to inaccurate predictions of the binding energies and absorption spectra of realistic nanostructures.

Consequently, the primary aim of the present work is to develop a rigorous theoretical framework for hole states in NCSCSQDs using the Luttinger model. Based on this framework, we aim to calculate the exciton energies (accounting for both Coulomb and standard exchange interactions). Ultimately, this study determines the specific impact of the core's spatial non-concentricity on these fundamental electronic and optical parameters, providing a more realistic and comprehensive picture of these asymmetric nanostructures.

2. Theoretical Model of Hole States

2.1. Geometry of the nanostructure and the shape functions

We consider an NCSCSQD consisting of a core with radius r_0 surrounded by a shell with an outer radius r_1. The entire core-shell heterostructure is embedded in an infinite bulk matrix. We also assume that the geometric center of the core is shifted from the center of the spherical shell by a distance D along the z-direction (Fig. 1). We set the origin of our Cartesian coordinate system at the geometric center of the outer shell. Consequently, the displacement vector of the core is defined as $\mathbf{D} = (0, 0, D)$, where the physical condition for the core to remain entirely within the shell is $D \leq r_1 - r_0$.

The nanostructure therefore partitions the space into three regions with different material parameters: the core $\Omega_c = \{\mathbf{r} : |\mathbf{r} - \mathbf{D}| \leq r_0\}$; the shell $\Omega_s = \{\mathbf{r} : |\mathbf{r}| \leq r_1\} \setminus \Omega_c$, and the outer matrix $\Omega_m = \mathbb{R}^3 \setminus \{\mathbf{r} : |\mathbf{r}| \leq r_1\}$. It is convenient to describe this partition by two spatial shape functions, each of which equals unity inside the corresponding sphere and zero outside:

$$\chi_1(\mathbf{r}) = \Theta(r_1 - |\mathbf{r}|), \tag{1}$$

$$\chi_c(\mathbf{r}) = \Theta(r_0 - |\mathbf{r} - \mathbf{D}|), \tag{2}$$

where $\Theta(x)$ is the Heaviside step function. Because the core lies entirely inside the shell, the two shape functions are nested, $\chi_c(\mathbf{r})\chi_1(\mathbf{r}) = \chi_c(\mathbf{r})$. This nesting is precisely what allows an arbitrary piecewise-constant material parameter $f(\mathbf{r})$, which takes the values f_c, f_s, and f_m in the core, in the shell, and in the matrix, respectively, to be written as a strictly linear superposition of the two shape functions:

$$f(\mathbf{r}) = f_m + (f_s - f_m)\chi_1(\mathbf{r}) + (f_c - f_s)\chi_c(\mathbf{r}). \tag{3}$$

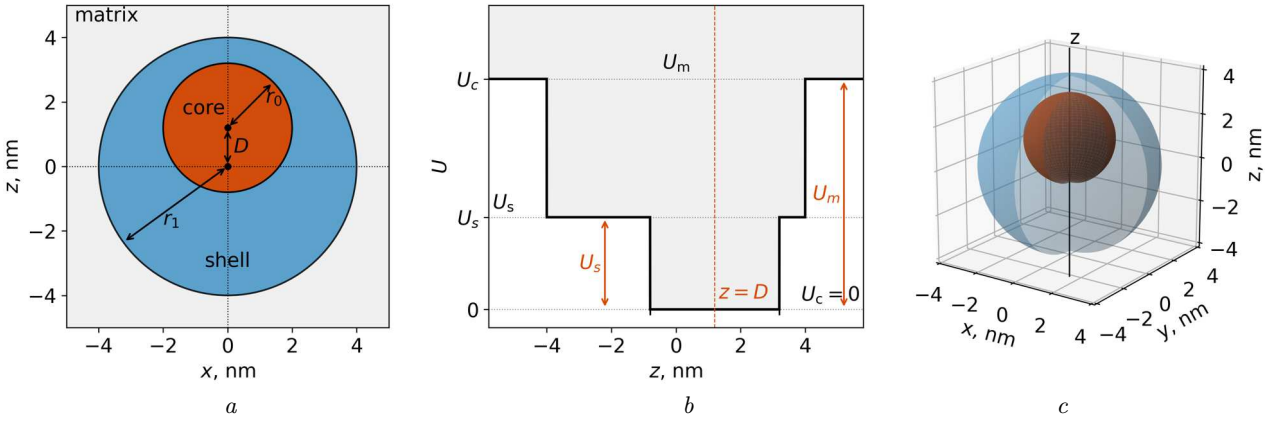

a *b* *c*

Fig. 1. Nonconcentric spherical core-shell quantum dot: cross-section in the XZ plane (a); confinement potential $U(0,0,z)$ (b); three-dimensional view with one quarter removed (c)

The first term (3) sets the background value of the matrix everywhere. The second term raises the parameter to its shell value over the whole volume of the outer sphere. The third term corrects the core region, where the parameter differs from that of the shell. Direct substitution confirms that (3) reproduces f_m for $\mathbf{r} \in \Omega_m$ ($\chi_1 = \chi_c = 0$), f_s for $\mathbf{r} \in \Omega_s$ ($\chi_1 = 1, \chi_c = 0$), and f_c for $\mathbf{r} \in \Omega_c$ ($\chi_1 = \chi_c = 1$). Therefore, the complete geometrical information about the nanostructure, including its non-concentricity, is carried by the pair of shape functions χ_1 and χ_c, whereas the material parameters are carried by the three numbers f_c, f_s, f_m. Every position-dependent quantity of the model obeys this single rule. In particular, the Luttinger parameters are

$$\gamma_1(\mathbf{r}) = \gamma_1^m + (\gamma_1^s - \gamma_1^m)\chi_1(\mathbf{r}) + (\gamma_1^c - \gamma_1^s)\chi_c(\mathbf{r}), \quad (4)$$

$$\gamma(\mathbf{r}) = \gamma^m + (\gamma^s - \gamma^m)\chi_1(\mathbf{r}) + (\gamma^c - \gamma^s)\chi_c(\mathbf{r}), \quad (5)$$

and the band offsets at the two heterointerfaces form the three-dimensional confining potential of the hole:

$$U(\mathbf{r}) = U_m + (U_s - U_m)\chi_1(\mathbf{r}) + (U_c - U_s)\chi_c(\mathbf{r}). \quad (6)$$

Here the top of the valence band of the core material is chosen as the reference level, $U_c = 0$; U_s is the valence-band offset at the core-shell interface and U_m is the barrier at the shell-matrix interface, with $0 < < U_s < U_m$. Hole energies are counted as positive into the valence band.

2.2. The hole Hamiltonian

In semiconductors with the zinc-blende structure the valence band is fourfold degenerate at the Γ point. The spin-orbit interaction splits the sixfold p-type manifold into the upper fourfold Γ_8 multiplet with the total angular momentum $j = 3/2$ and the lower twofold split-off Γ_7 band, separated by Δ_{so}. Since Δ_{so} considerably exceeds the confinement energies of the states considered below, the split-off band is neglected and the hole is described within the four-band Luttinger–Kohn model [16–18].

We neglect the corrugation of isoenergetic surfaces in k-space, i.e. we use the spherical Baldereschi–Lipari approximation [19] and replace the Luttinger parameters γ_2 and γ_3 with one effective spherical parameter, defined separately in each domain:

$$\gamma(\mathbf{r}) = \frac{2\gamma_2(\mathbf{r}) + 3\gamma_3(\mathbf{r})}{5}. \quad (7)$$

In this approximation, the kinetic energy operator commutes with the total angular momentum operator. Therefore, all spectral symmetry breaking arises solely from the geometry of the nanosystem.

For a spatially homogeneous material, the spherical Luttinger Hamiltonian has the compact Baldereschi–Lipari form:

$$\hat{H}_L = \frac{\hbar^2}{2m_0}\left[\left(\gamma_1 + \frac{5}{2}\gamma\right)\hat{k}^2 - 2\gamma\left(\hat{\mathbf{k}}\cdot\hat{\mathbf{J}}\right)^2\right], \quad (8)$$

where m_0 is the free-electron mass, $\hat{k}_\alpha = -i\,\partial/\partial x_\alpha$ and $\hat{J}_\alpha$ ($\alpha \in \{x, y, z\}$) are the 4×4 angular-momentum matrices for 3/2. In our heterostructure, however, γ_1 and γ are position-dependent and do not commute with $\hat{\mathbf{k}}$. The naive product $\gamma(\mathbf{r})(\hat{\mathbf{k}}\cdot\hat{\mathbf{J}})^2$ is not Hermitian and does not conserve probability current

across the heterointerfaces. The operator must therefore be symmetrized, which is the multiband generalization of the BenDaniel–Duke prescription:

$$\hat{H}_h = \frac{\hbar^2}{2m_0} \sum_{\alpha,\beta} \hat{k}_\alpha \hat{K}_{\alpha\beta}(\mathbf{r}) \hat{k}_\beta + U(\mathbf{r}) \hat{I}_{4\times 4}, \tag{9}$$

with the 4×4 kernel:

$$\hat{K}_{\alpha\beta}(\mathbf{r}) = \left[\gamma_1(\mathbf{r}) + \frac{5}{2}\gamma(\mathbf{r})\right] \delta_{\alpha\beta} - \gamma(\mathbf{r}) \{\hat{J}_\alpha, \hat{J}_\beta\}, \tag{10}$$

where $\{\hat{A}, \hat{B}\} = \hat{A}\hat{B} + \hat{B}\hat{A}$ is the anticommutator and $\hat{I}_{4\times 4}$ is the identity matrix. The kernel is symmetric, $\hat{K}_{\alpha\beta} = \hat{K}_{\beta\alpha}$, and Hermitian for every $\mathbf{r}$. Consequently, $\hat{H}_h$ is Hermitian for arbitrary profiles $\gamma_1(\mathbf{r}), \gamma(\mathbf{r})$. For constant parameters, (9) reduces exactly to (8), because $\sum_{\alpha\beta} \hat{k}_\alpha \hat{k}_\beta \{\hat{J}_\alpha, \hat{J}_\beta\} = 2\gamma(\hat{\mathbf{k}} \cdot \hat{\mathbf{J}})^2$. Integrating (9) across a heterointerface reproduces the correct matching conditions, namely the continuity of the four-component envelope Ψ and of the generalized current $\sum_\beta \hat{K}_{\alpha\beta}(\mathbf{r}) \hat{k}_\beta \Psi$.

In the basis of the eigenstates $|3/2, m_j\rangle$ of $\hat{J}_z$, ordered as $m_j = 3/2, 1/2, -1/2, -3/2$, the Hamiltonian (9) takes the familiar Luttinger form:

$$\hat{H}_h = \begin{pmatrix} \hat{P}+\hat{Q} & -\hat{S} & \hat{R} & 0 \\ -\hat{S}^+ & \hat{P}-\hat{Q} & 0 & \hat{R} \\ \hat{R}^+ & 0 & \hat{P}-\hat{Q} & \hat{S} \\ 0 & \hat{R}^+ & \hat{S}^+ & \hat{P}+\hat{Q} \end{pmatrix} + U(\mathbf{r}) \hat{I}_{4\times 4}, \tag{11}$$

where

$$\begin{aligned} \hat{P} &= \frac{\hbar^2}{2m_0} \sum_\alpha \hat{k}_\alpha \gamma_1(\mathbf{r}) \hat{k}_\alpha, \\ \hat{Q} &= \frac{\hbar^2}{2m_0} \left[\hat{k}_x \gamma(\mathbf{r}) \hat{k}_x + \hat{k}_y \gamma(\mathbf{r}) \hat{k}_y - 2\hat{k}_z \gamma(\mathbf{r}) \hat{k}_z\right], \\ \hat{R} &= -\frac{\hbar^2}{2m_0} \sqrt{3}\, \hat{k}_- \gamma(\mathbf{r}) \hat{k}_-, \\ \hat{S} &= \frac{\hbar^2}{2m_0} \sqrt{3} \left[\hat{k}_z \gamma(\mathbf{r}) \hat{k}_- + \hat{k}_- \gamma(\mathbf{r}) \hat{k}_z\right], \end{aligned} \tag{12}$$

where $\hat{k}_\pm = \hat{k}_x \pm i\hat{k}_y$. The operators $\hat{P}$ and $\hat{Q}$ are self-adjoint, whereas $\hat{R}$ and $\hat{S}$ are not, and the lower triangular part of (11) contains their adjoints, which must be written out explicitly:

$$\begin{aligned} \hat{R}^+ &= -\frac{\hbar^2}{2m_0} \sqrt{3}\, \hat{k}_+ \gamma(\mathbf{r}) \hat{k}_+, \\ \hat{S}^+ &= \frac{\hbar^2}{2m_0} \sqrt{3} \left[\hat{k}_z \gamma(\mathbf{r}) \hat{k}_+ + \hat{k}_+ \gamma(\mathbf{r}) \hat{k}_z\right]. \end{aligned} \tag{13}$$

Eqs (12) and (13) follow from (10) by direct evaluation of the anticommutators $\{\hat{J}_\alpha, \hat{J}_\beta\}_{m_j m_j'}$. The adjoints are obtained from the elementary rules $\hat{k}_\alpha^+ = \hat{k}_\alpha$, $\hat{k}_\pm^+ = \hat{k}_\mp$, together with the fact that $\gamma(\mathbf{r})$ is real, so that $(\hat{k}_\mu \gamma \hat{k}_\nu)^+ = \hat{k}_\nu^+ \gamma \hat{k}_\mu^+$.

2.3. The plane-wave expansion and the matrix elements

According to the plane wave expansion method, we assume that the NCSCSQD is placed inside a large cubic supercell of volume $\Omega = L^3$ and periodic Born–von Karman boundary conditions are imposed. The edge $L > 2.5\, r_1 + a_b^*$ [20, 21] (where a_b^* is the effective Bohr radius) is chosen large enough for the exponential tail of the hole wave function penetrating into the matrix to decay completely within the supercell, so that the spurious interaction between adjacent periodic images and the artificial confinement by the supercell boundary are both negligible. The four-component hole envelope is then expanded in an orthonormal plane-wave basis:

$$\begin{aligned} \Psi(\mathbf{r}) &= \sum_{\mathbf{G}, m_j} C_{\mathbf{G}, m_j} |\mathbf{G}, m_j\rangle, \\ |\mathbf{G}, m_j\rangle &= \frac{1}{\sqrt{\Omega}} e^{i\mathbf{G}\cdot\mathbf{r}} |m_j\rangle, \end{aligned} \tag{14}$$

where $m_j \in \{3/2, 1/2, -1/2, -3/2\}$. $C_{\mathbf{G}, m_j}$ are unknown coefficients, and the reciprocal lattice vectors of the supercell are

$$\mathbf{G} = \frac{2\pi}{L}(n_x, n_y, n_z), \quad n_i \in \mathbb{Z}. \tag{15}$$

During the calculation, the basis is truncated by retaining only those $\mathbf{G}$ that satisfy the isotropic condition:

$$n_x^2 + n_y^2 + n_z^2 \le N_{\text{cut}}^2, \tag{16}$$

where N_{cut} is a convergence parameter. The main advantage of this representation is that the boundary conditions at both heterointerfaces need not be imposed by hand. They are automatically accounted for through the Fourier transforms of the material parameters.

The whole construction rests on a single identity. For an arbitrary function $f(\mathbf{r})$ that is periodic over the supercell, the matrix element of the symmetrized operator $\hat{k}_\alpha f(\mathbf{r}) \hat{k}_\beta$ is

$$\langle \mathbf{G} | \hat{k}_\alpha f(\mathbf{r}) \hat{k}_\beta | \mathbf{G}' \rangle = G_\alpha G'_\beta \tilde{f}(\mathbf{q}), \quad \mathbf{q} = \mathbf{G} - \mathbf{G}', \tag{17}$$

where the Fourier transform is defined as

$$\tilde{f}(\mathbf{q}) = \frac{1}{\Omega}\int\limits_{\Omega} f(\mathbf{r}) e^{-i\mathbf{q}\cdot\mathbf{r}}\, d^3r. \tag{18}$$

To obtain (17) it suffices to note that $\hat{k}_\beta$ acting to the right on $e^{i\mathbf{G}'}\cdot\mathbf{r}$ produces the factor G'_β, while $\hat{k}_\alpha$ is transferred onto the left exponential by integration by parts, with the surface term vanishing by virtue of the periodic boundary conditions, thereby producing the factor G_α. Thus the non-commutativity of $\hat{\mathbf{k}}$ and $f(\mathbf{r})$ is resolved exactly, without any approximation, and no derivative of the discontinuous parameters ever needs to be evaluated. Since $\hat{k}_\pm$ are mere linear combinations of $\hat{k}_x$ and $\hat{k}_y$, the rule (18) extends to the entries (12) of the Luttinger matrix. For instance, $\langle\mathbf{G}|\hat{k}_-\gamma(\mathbf{r})\hat{k}_-|\mathbf{G}'\rangle = G_-G'_-\tilde{\gamma}(\mathbf{q})$ with $G_\pm = G_x \pm iG_y$. Every operator in (12)–(13) thus turns into an algebraic bilinear form in the pair $(\mathbf{G},\mathbf{G}')$, which is what makes the whole Hamiltonian matrix analytic.

Substituting the expansion (14) into the Schrödinger equation $\hat{H}_h\Psi = E\Psi$, projecting onto the basis, and applying (17) to the kernel (10), we arrive at the algebraic eigenvalue problem:

$$\sum_{\mathbf{G}',m'_j} H_{m_jm'_j}(\mathbf{G},\mathbf{G}')C_{\mathbf{G}',m'_j} = EC_{\mathbf{G},m_j} \tag{19}$$

with the matrix elements

$$H_{m_jm'_j}(\mathbf{G},\mathbf{G}') = \frac{\hbar^2}{2m_0}\left(\tilde{\gamma}_1(\mathbf{q}) + \frac{5}{2}\tilde{\gamma}(\mathbf{q})\right)\times$$

$$\times\,(\mathbf{G}\cdot\mathbf{G}')\delta_{m_jm'_j} - \frac{\hbar^2}{2m_0}\tilde{\gamma}(\mathbf{q})\times$$

$$\times\left\langle m_j\middle|\left\{(\mathbf{G}\cdot\hat{\mathbf{J}}),(\mathbf{G}'\cdot\hat{\mathbf{J}})\right\}\middle|m'_j\right\rangle + \tilde{U}(\mathbf{q})\delta_{m_jm'_j}, \tag{20}$$

where $\mathbf{q} = \mathbf{G} - \mathbf{G}'$ and $\tilde{\gamma}_1(\mathbf{q})$, $\tilde{\gamma}(\mathbf{q})$, $\tilde{U}(\mathbf{q})$ denote the Fourier transforms (18) of the corresponding position-dependent quantities. Eq. (20) is the exact plane-wave image of the Hamiltonian (9). Its Hermiticity is manifest: $\mathbf{G}\cdot\mathbf{G}'$ is symmetric under $\mathbf{G}\leftrightarrow\mathbf{G}'$, the anticommutator obeys $\{\hat{A},\hat{B}\} = \{\hat{B},\hat{A}\}$ and is Hermitian for real $\mathbf{G}$, and, since $\gamma(\mathbf{r})$ and $U(\mathbf{r})$ are real, $\tilde{\gamma}(-\mathbf{q}) = \tilde{\gamma}^*(\mathbf{q})$ and $\tilde{U}(-\mathbf{q}) = \tilde{U}^*(\mathbf{q})$. Taken together, these give $H_{m_jm'_j}(\mathbf{G},\mathbf{G}') = [H_{m'_jm_j}(\mathbf{G}',\mathbf{G})]^*$.

Written out explicitly, (20) preserves the block structure,

$$\hat{H}(\mathbf{G},\mathbf{G}') = \begin{pmatrix} P+Q & -S & R & 0\\ -\bar{S} & P-Q & 0 & R\\ \bar{R} & 0 & P-Q & S\\ 0 & \bar{R} & \bar{S} & P+Q\end{pmatrix} + \\ + \tilde{U}(\mathbf{q})\hat{I}_{4\times4}, \tag{21}$$

where each entry is the plane-wave matrix element of the corresponding operator in (12)–(13),

$$\begin{aligned} P &= \langle\mathbf{G}|\hat{P}|\mathbf{G}'\rangle, \quad Q = \langle\mathbf{G}|\hat{Q}|\mathbf{G}'\rangle,\\ R &= \langle\mathbf{G}|\hat{R}|\mathbf{G}'\rangle, \quad \bar{R} = \langle\mathbf{G}|\hat{R}^\dagger|\mathbf{G}'\rangle,\\ S &= \langle\mathbf{G}|\hat{S}|\mathbf{G}'\rangle, \quad \bar{S} = \langle\mathbf{G}|\hat{S}^\dagger|\mathbf{G}'\rangle, \end{aligned} \tag{22}$$

so that the barred symbols are a shorthand for the adjoint operators and not for complex conjugation. Applying the identity (17) term by term, these bilinear forms are obtained in closed form:

$$\begin{aligned} P(\mathbf{G},\mathbf{G}') &= \frac{\hbar^2}{2m_0}\tilde{\gamma}_1(\mathbf{q})(\mathbf{G}\cdot\mathbf{G}'),\\ Q(\mathbf{G},\mathbf{G}') &= \frac{\hbar^2}{2m_0}\tilde{\gamma}(\mathbf{q})(G_xG'_x + G_yG'_y - 2G_zG'_z),\\ R(\mathbf{G},\mathbf{G}') &= -\frac{\hbar^2}{2m_0}\sqrt{3}\,\tilde{\gamma}(\mathbf{q})G_-G'_-,\\ \bar{R}(\mathbf{G},\mathbf{G}') &= -\frac{\hbar^2}{2m_0}\sqrt{3}\,\tilde{\gamma}(\mathbf{q})G_+G'_+,\\ S(\mathbf{G},\mathbf{G}') &= \frac{\hbar^2}{2m_0}\sqrt{3}\,\tilde{\gamma}(\mathbf{q})(G_zG'_- + G'_zG_-),\\ \bar{S}(\mathbf{G},\mathbf{G}') &= \frac{\hbar^2}{2m_0}\sqrt{3}\,\tilde{\gamma}(\mathbf{q})(G_zG'_+ + G'_zG_+). \end{aligned} \tag{23}$$

Eqs (23) make the Hermitian structure fully explicit. The barred quantities obey

$$\begin{aligned} \bar{R}(\mathbf{G},\mathbf{G}') &= [R(\mathbf{G}',\mathbf{G})]^*,\\ \bar{S}(\mathbf{G},\mathbf{G}') &= [S(\mathbf{G}',\mathbf{G})]^*, \end{aligned} \tag{24}$$

that is, the arguments have to be interchanged together with the complex conjugation, which is the plane-wave image of the operator adjoints (13).

Applying the definition (18) to the decomposition (3), we obtain, for any parameter of the model:

$$\tilde{f}(\mathbf{q}) = f_m\delta_{\mathbf{q},0} + (f_s - f_m)\tilde{\chi}_1(\mathbf{q}) + (f_c - f_s)\tilde{\chi}_c(\mathbf{q}). \tag{25}$$

Consequently, the whole problem reduces to the evaluation of the two Fourier transforms $\tilde{\chi}_1(\mathbf{q})$ and $\tilde{\chi}_c(\mathbf{q})$, both of which are obtained analytically.

Consider first a sphere of radius R centered at the origin. Since its shape function depends only on $|\mathbf{r}|$, we may align $\mathbf{q}$ with the polar axis without loss of generality, so that $\mathbf{q}\cdot\mathbf{r} = qr\cos\theta$ with $q = |\mathbf{q}|$. Switching to spherical coordinates,

$$\int\limits_{|\mathbf{r}|\le R} e^{-i\mathbf{q}\cdot\mathbf{r}} d^3r = \int\limits_0^R r^2 dr \int\limits_0^{2\pi} d\phi \int\limits_0^{\pi} e^{-iqr\cos\theta}\sin\theta\, d\theta. \quad (26)$$

The angular integration gives $\int_0^{\pi} e^{-iqr\cos\theta}\sin\theta\, d\theta = 2\sin(qr)/(qr)$, and the remaining radial integral $(4\pi/q)\int_0^R r\sin(qr)\, dr$ is elementary. Hence

$$F(q,R) = \int\limits_{|\mathbf{r}|\le R} e^{-i\mathbf{q}\cdot\mathbf{r}} d^3r = \begin{cases} \dfrac{4\pi}{q^3}\big[\sin(qR) - qR\cos(qR)\big], & q \neq 0, \\ \dfrac{4\pi R^3}{3}, & q = 0, \end{cases} \quad (27)$$

the second line following from the limit $q \to 0$ of the first and coinciding, as it must, with the volume of the sphere. The function $F(q,R)$ is real and depends only on $|\mathbf{q}|$.

The shell sphere is centered at the origin; therefore,

$$\tilde{\chi}_1(\mathbf{q}) = \frac{1}{\Omega} F(q, r_1). \quad (28)$$

The core sphere, by contrast, is centered at $\mathbf{D} = (0,0,D)$. Performing the substitution $\mathbf{r} = \mathbf{r}' + \mathbf{D}$ in (18) and using the shift theorem, we get

$$\tilde{\chi}_c(\mathbf{q}) = \frac{1}{\Omega} \int\limits_{|\mathbf{r}-\mathbf{D}|\le r_0} e^{-i\mathbf{q}\cdot\mathbf{r}} d^3r = \frac{1}{\Omega} e^{-i\mathbf{q}\cdot\mathbf{D}} \int\limits_{|\mathbf{r}'|\le r_0} e^{-i\mathbf{q}\cdot\mathbf{r}'} d^3r' = \frac{1}{\Omega} e^{-iq_z D} F(q, r_0). \quad (29)$$

Eqs (28)–(29) constitute the central analytic result of the model. The displacement of the core enters the entire formalism exclusively through the phase factor $\exp(-iq_z D)$. The moduli of the Fourier harmonics are independent of D. Therefore, the whole physics of the non-concentricity is encoded in the relative phases between the harmonics, which is precisely what destroys the spherical symmetry of the confining potential and of the effective-mass profile while leaving their magnitudes intact. For $D = 0$ all Fourier coefficients become real and even functions of $\mathbf{q}$, and the concentric core-shell QD is recovered as a special case of the same formulae. The limit $r_0 \to 0$, or $\gamma^c = \gamma^s$, $\gamma_1^c = \gamma_1^s$, $U_s = 0$, yields a homogeneous spherical QD. Both limits provide a convenient test of the numerical implementation.

Collecting (25)–(29), the Fourier transforms that enter the matrix elements (20) are given analytically by

$$\tilde{\gamma}_1(\mathbf{q}) = \gamma_1^m \delta_{\mathbf{q},0} + \frac{1}{\Omega}\Big[(\gamma_1^s - \gamma_1^m)F(q,r_1) + (\gamma_1^c - \gamma_1^s)e^{-iq_z D}F(q,r_0)\Big], \quad (30)$$

$$\tilde{\gamma}(\mathbf{q}) = \gamma^m \delta_{\mathbf{q},0} + \frac{1}{\Omega}\Big[(\gamma^s - \gamma^m)F(q,r_1) + (\gamma^c - \gamma^s)e^{-iq_z D}F(q,r_0)\Big], \quad (31)$$

$$\tilde{U}(\mathbf{q}) = U_m \delta_{\mathbf{q},0} + \frac{1}{\Omega}\Big[(U_s - U_m)F(q,r_1) - U_s e^{-iq_z D}F(q,r_0)\Big], \quad (32)$$

where the last equality accounts for the chosen reference level $U_c = 0$. For $\mathbf{q} = \mathbf{0}$, the Kronecker symbol contributes, and (29) yields the volumes of the two spheres, $F(0,r_1) = V_1 = 4\pi r_1^3/3$ and $F(0,r_0) = V_c = 4\pi r_0^3/3$, so that the diagonal harmonics reduce to the volume-averaged parameters of the supercell, for example,

$$\tilde{\gamma}_1(0) = \gamma_1^m + (\gamma_1^s - \gamma_1^m)\frac{V_1}{\Omega} + (\gamma_1^c - \gamma_1^s)\frac{V_c}{\Omega}, \quad (33)$$

which resolves the apparent divergence of (29) at $q \to 0$ and provides an additional consistency check of the construction.

A remark on the Luttinger parameters of the matrix is in order. The wide-gap host has no valence band structure that could be described by the same Γ_8 manifold, and its Luttinger parameters are, strictly speaking, not defined. We therefore set $\gamma_1^m = 1$ and $\gamma^m = 0$, which reduces the kernel (10) in the matrix to $\hat{K}_{\alpha\beta} = \delta_{\alpha\beta}\hat{I}_{4\times4}$, i.e., to a free particle of mass m_0 moving in the barrier U_m. This choice is physically justified because the high barrier confines the hole almost entirely within the heterostructure, so that the details of the dispersion in the matrix are irrelevant, while the four components of the envelope decouple in the barrier and decay as $\exp\big(-\sqrt{2m_0(U_m - E)}\, r/\hbar\big)$, as expected.

3. Theoretical Model of Electron States

The description of the exciton requires the electron states as well. The conduction band of the materials considered is nondegenerate and isotropic near the Γ point, so that the electron is adequately described by the single-band effective-mass approximation with the Hamiltonian written in the BenDaniel–Duke form,

$$\hat{H}_e = -\frac{\hbar^2}{2}\boldsymbol{\nabla}\cdot\left[\frac{1}{m_e^*(\mathbf{r})}\boldsymbol{\nabla}\right] + U_e(\mathbf{r}) =$$

$$= \frac{\hbar^2}{2}\sum_\alpha \hat{k}_\alpha \frac{1}{m_e^*(\mathbf{r})}\hat{k}_\alpha + U_e(\mathbf{r}). \tag{34}$$

Both the inverse effective mass $1/m_e^*(\mathbf{r})$ and the electron confining potential $U_e(\mathbf{r})$ are piecewise-constant and therefore obey the same decomposition (3). Expanding the electron envelope over the scalar plane-wave basis, $\psi(\mathbf{r}) = \Omega^{-1/2}\sum_{\mathbf{G}} A_{\mathbf{G}} e^{i\mathbf{G}\cdot\mathbf{r}}$, and applying the same identity (18), we obtain the matrix elements in closed form,

$$H_e(\mathbf{G},\mathbf{G}') = \frac{\hbar^2}{2}(\mathbf{G}\cdot\mathbf{G}')\tilde{\eta}(\mathbf{q}) + \tilde{U}_e(\mathbf{q}), \tag{35}$$

where $\tilde{\eta}(\mathbf{q})$ and $\tilde{U}_e(\mathbf{q})$ are given by (25) with the same functions (29) and (30). Thus the electron and the hole problems are treated on exactly the same footing and share the same analytic Fourier transforms. Electron states in the NCSCSQD have been calculated and analyzed in detail in [11, 12]. The only difference is the scalar rather than four-component structure of the basis. The electron levels $E_\mu^{(e)}$ and the coefficients $A_{\mathbf{G}}^{(\mu)}$ obtained from (35) serve, together with the hole states, as the single-particle basis for the exciton problem considered below.

4. Theoretical Model of Exciton States

4.1. The exciton Hamiltonian

The single-particle spectra of Secs. 2 and 3 describe an electron and a hole that do not feel each other. In a strongly confined nanocrystal, however, the Coulomb attraction between the photocreated carriers is comparable to the confinement energies and cannot be treated as a weak perturbation, while the short-range electron-hole exchange interaction, although much smaller in magnitude, is the only term that removes the spin degeneracy of the pair and therefore determines which of the exciton levels are optically active. Both terms must be included, and both are added to the sum of the single-particle Hamiltonians:

$$\hat{H}_{\rm ex} = \hat{H}_e + \hat{H}_h + \hat{V}_{\rm C}(\mathbf{r}_e,\mathbf{r}_h) + \hat{H}_{\rm exch}, \tag{36}$$

where $\hat{H}_e$ is given by Eq. (34) and $\hat{H}_h$ by Eq. (9). The direct Coulomb term is

$$\hat{V}_{\rm C}(\mathbf{r}_e,\mathbf{r}_h) = -\frac{e^2}{4\pi\varepsilon_0\varepsilon|\mathbf{r}_e-\mathbf{r}_h|}, \tag{37}$$

in which ε is the effective static dielectric constant of the heterostructure. Since the core and the shell are made of different materials, we take ε to be the volume-weighted average over the two regions,

$$\varepsilon = \frac{\varepsilon_c V_c + \varepsilon_s(V_1 - V_c)}{V_1},$$
$$V_c = \frac{4\pi r_0^3}{3}, \quad V_1 = \frac{4\pi r_1^3}{3}, \tag{38}$$

which uses the same two volumes that already appeared in the $\mathbf{q} = 0$ limit (33) of the Fourier transforms. This simplification is justified because a fully consistent treatment of a position-dependent $\varepsilon(\mathbf{r})$ would require the solution of the Poisson equation with the polarization charges induced at both heterointerfaces, which lies beyond the scope of the present work. In addition, we consider QDs for which the difference in dielectric constants is small.

The exchange term requires more care than in the single-band description. Because the hole is described by the four-band Luttinger model, it carries the angular momentum $j = 3/2$ rather than a spin 1/2, and the electron-hole exchange is not of the $(\hat{\boldsymbol{\sigma}}_e \times \hat{\boldsymbol{\sigma}}_h)$ singlet-triplet type. The short-range exchange interaction between a Γ_6 electron and a Γ_8 hole is instead the standard contact operator [22]:

$$\hat{H}_{\rm exch} = -\frac{2}{3}\varepsilon_{\rm exch}(\mathbf{r}_e)\, a_0^3\, \delta(\mathbf{r}_e - \mathbf{r}_h)\left(\hat{\boldsymbol{\sigma}} \times \hat{\mathbf{J}}\right), \tag{39}$$

where $\hat{\boldsymbol{\sigma}}$ are the Pauli matrices acting on the electron spin, $\hat{\mathbf{J}}$ are the same 4×4 angular-momentum matrices for 3/2 that enter the Luttinger kernel (10), a_0 is the lattice constant, and $\varepsilon_{\rm exch}$ is the bulk exciton exchange constant. The δ-function expresses the fact that the exchange is a short-range interaction acting on the scale of the unit cell. Since $\varepsilon_{\rm exch}$ differs appreciably between the core and the shell materials, we

keep it position-dependent; being piecewise-constant, it obeys the same decomposition (3) as every other parameter of the model,

$$\varepsilon_{\text{exch}}(\mathbf{r}) = \varepsilon^{m}_{\text{exch}} + (\varepsilon^{s}_{\text{exch}} - \varepsilon^{m}_{\text{exch}})\,\chi_1(\mathbf{r}) + \\ + (\varepsilon^{c}_{\text{exch}} - \varepsilon^{s}_{\text{exch}})\,\chi_c(\mathbf{r}), \tag{40}$$

so that its Fourier transform is again given analytically by (25), (28) and (29).

4.2. The exciton basis and the wave function

The single-particle Hamiltonian (34) of the electron contains no spin-orbit coupling, so each electron level $E^{(e)}_{\mu}$ with the envelope $\psi_\mu(\mathbf{r}_e)$ is twofold degenerate with respect to the spin projection $s_z = \pm 1/2$, and the spatial and spin variables of the electron factorize. The hole, by contrast, is not a product of an envelope and a spinor, because the state ν obtained by diagonalization of (20) is an irreducible four-component object

$$\Psi_\nu(\mathbf{r}_h) = \textstyle\sum_{m_j} \Psi_{\nu,m_j}(\mathbf{r}_h)|3/2, m_j), \\ \Psi_{\nu,m_j}(\mathbf{r}_h) = \dfrac{1}{\sqrt{\Omega}} \displaystyle\sum_{\mathbf{G}} C^{(\nu)}_{\mathbf{G},m_j} e^{i\mathbf{G}\cdot\mathbf{r}_h}, \tag{41}$$

in which the Bloch index m_j is inseparably entangled with the spatial dependence through the plane-wave coefficients $C^{(\nu)}_{\mathbf{G},m_j}$. This is the essential structural difference from the single-band description, and it carries over to every subsequent step.

The non-interacting electron-hole configurations $|\mu s_z) \otimes |\nu)$ therefore form the natural basis of the exciton problem, and the exciton wave function is the full configuration interaction expansion

$$\Psi^{(n)}_{\text{ex}}(\mathbf{r}_e, \sigma_e; \mathbf{r}_h) = \sum_{\mu,\nu} \sum_{s_z} C^{(n)}_{\mu s_z,\nu} \times \\ \times \psi_\mu(\mathbf{r}_e)|s_z) \otimes \Psi_\nu(\mathbf{r}_h), \tag{42}$$

or

$$\Psi^{(n)}_{\text{ex}} = \sum_{\mu,\nu} \sum_{s_z,m_j} C^{(n)}_{\mu s_z,\nu} \psi_\mu(\mathbf{r}_e) \times \\ \times \Psi_{\nu,m_j}(\mathbf{r}_h)|s_z)|3/2, m_j). \tag{43}$$

The coefficients $C^{(n)}_{\mu s_z,\nu}$ carry no m_j index: the distribution of the hole over the four Bloch components is already fixed by the single-particle state ν. If N_e electron and N_h hole levels are retained, the exciton matrix has dimensions $2N_eN_h \times 2N_eN_h$.

Projecting (36) onto this basis gives the secular problem

$$\sum_{\mu' s'_z \nu'} H^{\text{ex}}_{\mu s_z \nu,\mu' s'_z \nu'} C^{(n)}_{\mu' s'_z,\nu'} = E_n C^{(n)}_{\mu s_z,\nu}, \tag{44}$$

with

$$H^{\text{ex}}_{\mu s_z \nu,\mu' s'_z \nu'} = \big(E^{(e)}_{\mu} + E^{(h)}_{\nu}\big)\delta_{\mu\mu'}\delta_{\nu\nu'}\delta_{s_z s'_z} + \\ + W_{\mu\nu,\mu'\nu'}\delta_{s_z s'_z} + K^{\text{exch}}_{\mu s_z \nu,\mu' s'_z \nu'}. \tag{45}$$

The first term is diagonal and contains the single-particle spectra of Secs. 2 and 3. The second term, the Coulomb interaction, acts only on the spatial coordinates and is therefore diagonal in the electron spin, but it couples different configurations (μ, ν). The third term is the only one that mixes the spin channels. The two remaining subsections reduce W and K^{exch} to closed-form expressions in the plane-wave coefficients.

4.3. Matrix elements of the Coulomb interaction

Since the supercell is periodic, the Coulomb kernel is expanded in the same discrete Fourier series as every other quantity of the model,

$$\frac{1}{|\mathbf{r}_e - \mathbf{r}_h|} = \frac{1}{\Omega} \sum_{\mathbf{p}} \frac{4\pi}{p^2} e^{i\mathbf{p}\cdot(\mathbf{r}_e - \mathbf{p}_h)}, \\ \hat{V}_{\text{C}} = -\frac{e^2}{\varepsilon_0 \varepsilon \Omega} \sum_{\mathbf{p}\neq 0} \frac{1}{p^2} e^{i\mathbf{p}\cdot(\mathbf{p}_e - \mathbf{p}_h)}, \tag{46}$$

where $\mathbf{p}$ runs over the reciprocal lattice of the supercell and $p = |\mathbf{p}|$. The term $\mathbf{p} = 0$ is excluded because it describes the interaction of the two uniform charge densities and is exactly cancelled by the neutralizing background, as it must be for a charge-neutral electron-hole pair.

The structure of (46) shows that the only quantities needed are the matrix elements of $e^{\mp i\mathbf{p}\cdot\mathbf{r}}$ between single-particle states, i.e., the transition densities in reciprocal space. For the electron and the hole, respectively, they are

$$\rho^{(e)}_{\mu\mu'}(\mathbf{p}) \equiv \langle \psi_\mu | e^{-i\mathbf{p}\cdot\mathbf{r}} | \psi_{\mu'} \rangle = \\ = \textstyle\sum_{\mathbf{G}} \big(A^{(\mu)}_{\mathbf{G}}\big)^* A^{(\mu')}_{\mathbf{G}+\mathbf{p}}, \\ \rho^{(h)}_{\nu\nu'}(\mathbf{p}) \equiv \langle \Psi_\nu | e^{-i\mathbf{p}\cdot\mathbf{r}} | \Psi_{\nu'} \rangle = \\ = \textstyle\sum_{\mathbf{G}} \sum_{m_j} \big(C^{(\nu)}_{\mathbf{G},m_j}\big)^* C^{(\nu')}_{\mathbf{G}+\mathbf{p},m_j}. \tag{47}$$

These equations are obtained by inserting the plane-wave expansions (14) and (41) and using the orthogonality $\Omega^{-1}\int_\Omega e^{i(\mathbf{G}'-\mathbf{G}-\mathbf{p})\cdot\mathbf{r}}d^3r=\delta_{\mathbf{G}',\mathbf{G}+\mathbf{p}}$, which collapses the double sum over the reciprocal lattice into a single one. Note that the hole density in (47) is summed over m_j. The Coulomb operator is proportional to the unit matrix in the Bloch subspace and cannot change the Bloch index. Both densities obey

$$\rho^{(i)}_{\alpha\beta}(-\mathbf{p})=\big[\rho^{(i)}_{\beta\alpha}(\mathbf{p})\big]^*,\quad i=e,h, \tag{48}$$

so that only one half of the $\mathbf{p}$ shell has to be stored.

Collecting Eqs (46)–(47) and observing that the electron and the hole absorb opposite momenta $\mp\hbar\mathbf{p}$, the six-dimensional integral of the direct Coulomb interaction reduces to a single discrete convolution over the reciprocal lattice

$$W_{\mu\nu,\mu'\nu'}=-\frac{e^2}{\varepsilon_0\varepsilon\Omega}\sum_{\mathbf{p}\neq0}\frac{1}{p^2}\,\rho^{(e)}_{\mu\mu'}(\mathbf{p})\,\rho^{(h)}_{\nu\nu'}(-\mathbf{p}). \tag{49}$$

Hermiticity, $W_{\mu\nu,\mu'\nu'}=[W_{\mu'\nu',\mu\nu}]^*$, follows directly from Eq. (48) together with the evenness of $1/p^2$. Thus no six-dimensional numerical integration is ever performed. The whole Coulomb problem is treated algebraically in the plane-wave coefficients, exactly as the single-particle problem was.

4.4. Matrix elements of the exchange interaction

The exchange operator (39) factorizes into a purely spin part and a purely spatial part. Substituting Eqs (39) and (43) and integrating the δ-function, which collapses the six-dimensional integral onto the diagonal $\mathbf{r}_e=\mathbf{r}_h=\mathbf{r}$, we obtain

$$K^{\mathrm{exch}}_{\mu s_z\nu,\mu' s'_z\nu'}=-\frac{2}{3}a_0^3\sum_{m_j,m'_j}\langle s_z,m_j|\hat{\boldsymbol{\sigma}}\cdot\hat{\mathbf{J}}|s'_z,m'_j\rangle\,I^{m_jm'_j}_{\mu\nu,\mu'\nu'}, \tag{50}$$

where the four-wave-function overlap integral, weighted by the position-dependent exchange constant, is

$$I^{m_jm'_j}_{\mu\nu,\mu'\nu'}=\int_\Omega\varepsilon_{\mathrm{exch}}(\mathbf{r})\,\psi^*_\mu(\mathbf{r})\psi_{\mu'}(\mathbf{r})\,\Psi^*_{\nu,m_j}(\mathbf{r})\times \\ \times\,\Psi_{\nu',m'_j}(\mathbf{r})\,d^3r. \tag{51}$$

In contrast to the Coulomb density (47), the hole indices m_j and m'_j are here not summed over. The operator $\hat{\boldsymbol{\sigma}}\times\hat{\mathbf{J}}$ is off-diagonal in the Bloch subspace, and it is exactly this off-diagonal structure that mixes the four hole components with the two electron spin states.

To evaluate Eq. (51), we introduce the m_j-resolved hole transition density,

$$\rho^{(h),m_jm'_j}_{\nu\nu'}(\mathbf{p})=\sum_{\mathbf{G}}\big(C^{(\nu)}_{\mathbf{G},m_j}\big)^*C^{(\nu')}_{\mathbf{G}+\mathbf{p},m'_j}, \\ \rho^{(h)}_{\nu\nu'}(\mathbf{p})=\sum_{m_j}\rho^{(h),m_jm_j}_{\nu\nu'}(\mathbf{p}), \tag{52}$$

where the second relation shows that the Coulomb density (48) is simply its trace. The products of two envelopes are then ordinary Fourier series determined by these densities

$$\psi^*_\mu(\mathbf{r})\psi_{\mu'}(\mathbf{r})=\frac{1}{\Omega}\sum_{\mathbf{p}}\rho^{(e)}_{\mu\mu'}(\mathbf{p})e^{i\mathbf{p}\cdot\mathbf{r}}, \\ \Psi^*_{\nu,m_j}(\mathbf{r})\Psi_{\nu',m'_j}(\mathbf{r})=\frac{1}{\Omega}\sum_{\mathbf{p}}\rho^{(h),m_jm'_j}_{\nu\nu'}(\mathbf{p})e^{i\mathbf{p}\cdot\mathbf{r}}, \tag{53}$$

and, inserting these together with the inverse transform $\varepsilon_{\mathrm{exch}}(\mathbf{r})=\sum_{\mathbf{q}}\tilde{\varepsilon}_{\mathrm{exch}}(\mathbf{q})e^{i\mathbf{q}\cdot\mathbf{r}}$ into (51) and integrating, we arrive at

$$I^{m_jm'_j}_{\mu\nu,\mu'\nu'}=\frac{1}{\Omega}\sum_{\mathbf{q}}\sum_{\mathbf{p}}\tilde{\varepsilon}_{\mathrm{exch}}(\mathbf{q})\,\rho^{(e)}_{\mu\mu'}(\mathbf{p})\times \\ \times\,\rho^{(h),m_jm'_j}_{\nu\nu'}(-\mathbf{q}-\mathbf{p}). \tag{54}$$

The three factors correspond to the momentum balance $\mathbf{q}+\mathbf{p}+(-\mathbf{q}-\mathbf{p})=0$. The inhomogeneity of the exchange constant supplies the momentum $\mathbf{q}$, while the electron and the hole exchange momentum $\mathbf{p}$. For a homogeneous exchange constant, $\tilde{\varepsilon}_{\mathrm{exch}}(\mathbf{q})=\varepsilon_{\mathrm{exch}}\delta_{\mathbf{q},0}$, and (54) collapses into a single convolution formally identical to the Coulomb expression (49) but with the kernel $1/p^2$ replaced by unity and with the term $\mathbf{p}=0$ retained,

$$I^{m_jm'_j}_{\mu\nu,\mu'\nu'}=\frac{\varepsilon_{\mathrm{exch}}}{\Omega}\sum_{\mathbf{p}}\rho^{(e)}_{\mu\mu'}(\mathbf{p})\,\rho^{(h),m_jm'_j}_{\nu\nu'}(-\mathbf{p}). \tag{55}$$

It remains to specify the spin factor of (50). In the product basis $|s_z\rangle|3/2,m_j\rangle$, the operator

$$\hat{\boldsymbol{\sigma}}\cdot\hat{\mathbf{J}}=\hat{\sigma}_z\hat{J}_z+\frac{1}{2}\big(\hat{\sigma}_+\hat{J}_-+\hat{\sigma}_-\hat{J}_+\big), \\ \hat{\sigma}_\pm=\hat{\sigma}_x\pm i\hat{\sigma}_y,\quad \hat{J}_\pm=\hat{J}_x\pm i\hat{J}_y, \tag{56}$$

is an 8×8 matrix whose non-zero elements connect the channels with $s_z+m_j=s'_z+m'_j$, i.e., it conserves

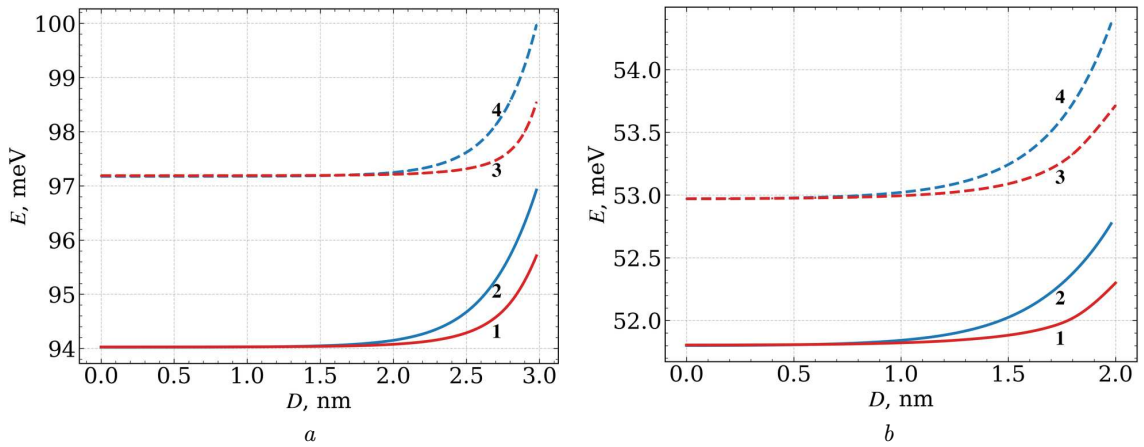

Fig. 2. Dependence of the two lowest hole multiplets on the core displacement D for a CdSe/CdS NCSCSQD with a fixed shell radius $r_1 = 5$ nm: core radius $r_0 = 2$ nm (*a*); core radius $r_0 = 3$ nm (*b*). Curves *1, 2* correspond to the ground multiplet; curves *3, 4* – to the first excited one. Within each multiplet, curves *1* and *3* are the states with $|F_z| = 3/2$, curves *2* and *4* – those with $|F_z| = 1/2$. Every curve is a Kramers doublet, so that the four curves represent eight hole states. At $D = 0$, the curves of each pair merge, recovering the fourfold degenerate multiplet of the concentric structure

the projection of the total angular momentum of the pair. All matrix elements of (50) are pure numbers, so that K^{exch} is obtained from (56) by a finite 4×4 contraction of the overlap integrals (54) with an 8×8 numerical matrix.

5. Results

The calculations were performed for a NCSCSQD embedded in an infinite matrix. The core displacement was varied over the whole physically admissible range, $0 \le D \le r_1 - r_0$. The following material parameters were used [23, 24]. For the core, $\gamma_1^c = 3.265\, m_0$, $\gamma_2^c = 1.162\, m_0$, $\gamma_3^c = 1.443\, m_0$ [23], which by (7) yields the spherical parameter $\gamma^c = 1.331\, m_0$. For the shell, $\gamma_1^s = 2.10\, m_0$, $\gamma_2^s = 0.70\, m_0$, $\gamma_3^s = 0.90\, m_0$, whence $\gamma^s = 0.82\, m_0$. For the matrix, we set $\gamma_1^m = 1$ and $\gamma^m = 0$, for the reasons discussed in Sec. 2.3. The top of the CdSe valence band is taken as the reference level, $U_c = 0$. The valence-band offset at the core-shell interface is $U_s = 450$ meV, consistent with the bulk band-gap difference $\Delta E_g \approx 750$ meV and a conduction-band offset of ≈ 0.3 eV reported for CdSe/CdS heterostructures [25, 27], and the barrier at the shell-matrix interface is $U_m = 4000$ meV. The static dielectric constants entering the effective value (38) are $\varepsilon_c = 5.8$ and $\varepsilon_s = 5.5$ [24–27]. Since these QDs are grown by colloidal synthesis, the surrounding matrix is a non-polar organic solvent with a considerably lower dielectric constant ($\varepsilon_m \approx 2.4$ for toluene [28]). It does not enter into (38), because the exciton is confined almost entirely within the heterostructure by the high barrier U_m, and the volume averaging in (38) is therefore restricted to the core and the shell.

First, we calculated the dependence of the hole energy on the location of the core for different core sizes and a fixed shell radius (Fig. 2). Since in the spherical approximation (7) the kinetic-energy operator commutes with the total angular momentum, it is convenient to classify the hole states by the total angular momentum operator $\hat{\mathbf{F}} = \hat{\mathbf{L}} + \hat{\mathbf{J}}$, where $\hat{\mathbf{L}}$ is the angular momentum associated with the envelope motion and $\hat{\mathbf{J}}$ is the operator of spin 3/2. For a concentric structure ($D = 0$), the confining potential (6) is spherically symmetric, both F and its projection F_z are good quantum numbers, and every level with a given F is $(2F+1)$-fold degenerate. A displacement of the core along the z-axis reduces the symmetry from spherical to axial. F ceases to be conserved, whereas the projection $F_z = m_j + m$ (where m is the azimuthal quantum number of the envelope component with the Bloch index m_j) remains a good quantum number for arbitrary D. Since F_z is half-integer, time-reversal invariance guarantees Kramers degeneracy $E(F_z) = E(-F_z)$, so that the states can be labelled by $|F_z|$ and each level remains at least twofold degenerate for any core displacement. At $D = 0$, the confining potential is spherically symmetric, and, accordingly, curves *1* and *2* in Fig. 2 start from a common

energy, and curves *3* and *4* likewise merge too. The exact coincidence of the branches in the concentric limit is a direct consequence of the spherical symmetry and simultaneously serves as an internal consistency check of the numerical method.

Displacing the core lowers the symmetry to axial. The projection F_z remains a good quantum number, but the degeneracy with respect to its modulus is lifted, and each fourfold multiplet splits into two Kramers doublets, $|F_z| = 3/2$ and $|F_z| = 1/2$. Kramers degeneracy is preserved for arbitrary D.

The splitting is strongly non-linear in D. Up to $D \approx 1.5$ nm for $r_0 = 2$ nm (and $D \approx 1.0$ nm for $r_0 = 3$ nm) the branches remain practically indistinguishable, and only when the core approaches the shell boundary does the splitting grow rapidly, reaching ≈ 1.2 meV for the ground multiplet and $\approx$1.5 meV for the excited one at the maximal displacement $D = r_1 - r_0 = 3$ nm (Fig. 2, *a*). This behaviour reflects the fact that a hole localized predominantly within the core is only weakly sensitive to the position of a distant interface. The perturbation becomes appreciable when the shell thickness on the side of the displacement becomes comparable with the penetration depth of the hole wave function into the barrier. The excited multiplet splits more strongly than the ground one, as its envelope extends further towards the shell boundary and therefore probes the induced anisotropy earlier.

Simultaneously, all branches shift upwards with increasing D, reflecting the enhanced confinement. A comparison of the two panels reveals the expected quantum size dependence. Increasing the core radius from 2 to 3 nm lowers the absolute energies by nearly a factor of two and reduces the splitting at the maximal admissible displacement from $\approx$1.2 to $\approx$0.5 meV, since a larger core leaves a thinner shell and hence a smaller range of accessible displacements.

Analogous calculations can be carried out for the electron states. Within the single-band effective-mass approximation (34), the conduction band is non-degenerate and isotropic near the Γ point, so the electron envelope is a scalar rather than a four-component object. Consequently, the electron levels carry no analogue of the F_z splitting discussed above. Each level remains twofold degenerate with respect to the spin projection $s_z = \pm 1/2$ for an arbitrary core displacement, but there is a splitting with respect to the azimuthal quantum number m_l [11, 12], and the effect of non-concentricity reduces to a monotonic shift of the levels. A detailed calculation and analysis of the electron energy spectrum in NCSCSQDs, including its dependence on the core displacement and on the geometrical parameters of the heterostructure, have been performed in [11, 12], and we therefore do not reproduce it here and use the electron levels and wave functions obtained there.

Having both single-particle spectra at our disposal, we can now turn to the exciton problem. The electron and hole states obtained above enter the configuration basis (42) of the full exciton Hamiltonian (36). It should be emphasised that the splitting of the hole multiplets described above does not simply carry over to the exciton spectrum. The Coulomb interaction mixes the configurations of electrons and holes, while the exchange operator (39) additionally couples the four hole components with the two electron spin states, so that the resulting exciton levels are classified by the projection of the total angular momentum of the electron-hole pair.

For the exciton calculation the geometry was fixed at a core radius $r_0 = 1.3$ nm and an outer shell radius $r_1 = 2.6$ nm. These dimensions were chosen to reproduce the CdSe/CdS sample S5 of the experimental study [9], so that the computed spectra can be compared directly with the measured data. In the concentric limit this corresponds to a shell thickness $r_1 - r_0 = 1.3$ nm, and the physically admissible range of the core displacement is therefore $0 \le D \le 1.3$ nm. The exciton wave function was expanded in the configuration basis (42) constructed from the $N_e = 3$ lowest electron levels (without spin) and the $N_h = 8$ lowest hole levels, which yields an exciton matrix of dimension $2N_eN_h = 48$ (including both electron and hole spins). This basis was found to be sufficiently converged for the ground and first excited exciton multiplets reported here.

Figure 3 shows the dependence of the two lowest exciton states on the core displacement D. These are the optically inactive (dark) and the optically active (bright, "light") states. Both branches shift monotonically to higher energy with increasing D, from $\approx$2123 meV (584 nm) in the concentric structure to $\approx$2173 meV ($\approx$571 nm) at the maximal displacement $D = 1.3$ nm, an overall blueshift of about 50 meV ($\approx$13 nm). This trend follows directly from the enhanced quantum confinement already identified for the single-particle hole spectrum. As the core ap-

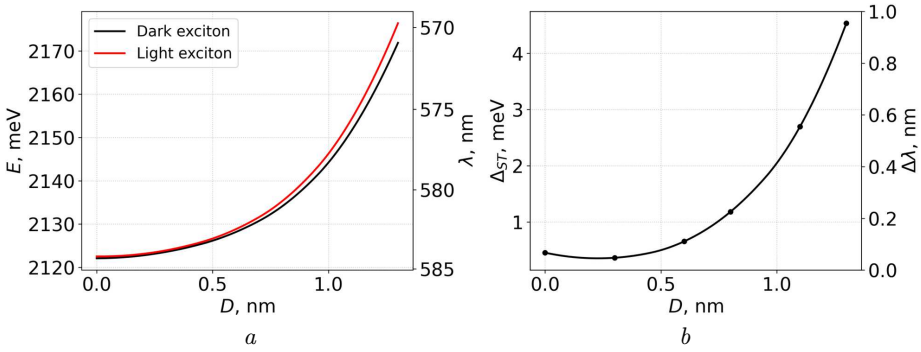

Fig. 3. Exciton energy and dark–light splitting in the NC-SCSQD as functions of the core displacement D: energy E and wavelength λ of the dark and light (bright) exciton states (a); dark–bright (singlet–triplet) splitting Δ_{ST} and the corresponding wavelength separation $\Delta\lambda$ (b)

proaches the shell boundary, the shell thickness on the displacement side becomes comparable with the penetration depth of the carrier envelopes, the electron and hole wave functions are compressed, and the single-particle confinement energies rise. Since this single-particle blueshift exceeds the concurrent, more modest increase in the Coulomb binding, the net exciton transition energy grows with D.

The absolute position of the transition provides a direct test against experiment. In our earlier work [12] the optical response of the same NCSCSQD was obtained from single-particle electron–hole transitions, i.e. neglecting both the Coulomb attraction and the electron-hole exchange. Within that approximation, the transition energy is essentially the single-particle gap E_e+E_h, which for the present geometry lies about 100 meV above the excitonic value and hence corresponds to a markedly shorter wavelength (≈560 nm), in poorer agreement with the measured absorption of sample S5. The direct Coulomb term, which for the exciton ground state amounts to ≈–97 meV at $D = 0$, redshifts the transition and brings the computed absorption edge to 584 nm, in quantitative agreement with the value reported in Ref. [9]. This demonstrates that the inclusion of excitonic effects is not merely a refinement but is essential for a realistic description of the optical response, and that it substantially improves the agreement with experiment relative to the single-particle treatment of Ref. [12].

The lower branch in Fig. 3 is the dark exciton, and the upper one is the bright exciton; their separation is the dark–bright (singlet–triplet) splitting Δ_{ST} produced by the short-range electron–hole exchange interaction (39). Even in the concentric QD ($D = 0$), the exchange already lifts the degeneracy of the band-edge multiplet [22], giving a small splitting $\Delta_{\mathrm{ST}} \approx 0.45$ meV. As the core is displaced, Δ_{ST} first passes through a shallow minimum near $D \approx 0.3$ nm and then rises steeply, reaching ≈4.5 meV at the maximal displacement $D = 1.3$ nm, which corresponds to a wavelength separation $\Delta\lambda$ of order 1 nm (Fig. 3, b). The growth of Δ_{ST} mirrors the behaviour of the exchange matrix elements (54)–(55). Displacing the core toward the shell boundary squeezes both carriers onto the thin-shell side and increases the electron-hole overlap that enters the contact exchange operator (39), so that the splitting grows accordingly. The same mechanism enhances the direct Coulomb binding, which strengthens from ≈–97 meV at $D = 0$ to ≈–101 meV at $D = 1.3$ nm. The exciton therefore becomes slightly more tightly bound as the non-concentricity increases.

Physically, the non-concentricity thus acts on the exciton in two distinct ways. It reduces the symmetry of the confining potential from spherical to axial, which (combined with the exchange interaction) is responsible for the dark–bright splitting and its pronounced enhancement at large D, while simultaneously enhancing the overall confinement and shifting the entire spectrum to higher energy. Because the resulting exciton levels are classified by the projection of the total angular momentum of the electron-hole pair rather than by the hole quantum number F_z alone, the hole-multiplet splitting discussed above does not carry over unchanged. The Coulomb and exchange couplings redistribute it among the exciton configurations, and the observable dark–bright splitting Δ_{ST} is the physically relevant fine-structure quantity.

6. Conclusions

We have developed a consistent theoretical framework for the electronic and excitonic states of non-concentric CdSe/CdS core-shell quantum dots, treat-

ing the valence band within the four-band Luttinger–Kohn model and incorporating the displaced-core potential exactly over the full range $0 \leq D \leq r_1 - r_0$. Non-concentricity acts as an effective symmetry-breaking field that lifts the degeneracy of the hole multiplet and produces a fine-structure splitting of the hole levels that grows monotonically with displacement.

The exciton states, obtained by configuration interaction including the direct Coulomb and short-range exchange interactions, are strongly tunable by the core displacement: the ground-state transition blueshifts by ≈50 meV as D increases, while the dark–bright splitting Δ_{ST} grows from ≈0.45 meV in the concentric dot to ≈4.5 meV at $D = 1.3$ nm. For the geometry of sample S5 of Ref. [9], the computed absorption edge falls at 584 nm, in quantitative agreement with experiment – an agreement reached only when excitonic effects are included, since the single-particle treatment of Ref. [12] overestimates the transition energy by ≈100 meV. Core displacement thus provides an effective means of tuning both the emission energy and the exciton fine structure of core–shell nanocrystals without changing their composition or size.

1. A. Sahu, D. Kumar. Core-shell quantum dots: A review on classification, materials, application, and theoretical modeling. *J. Alloys Compd.* **924**, 166508 (2022).
2. Y. Fu, J. Jussi, L. Elmlund, S. Dunne, Q. Wang, H. Brismar. Intrinsic blinking characteristics of single colloidal CdSe–CdS/ZnS core-multishell quantum dots. *Phys. Rev. B* **99**, 035404 (2019).
3. B. Omogo, F. Gao, P. Bajwa, M. Kaneko, C.D. Heyes. Reducing blinking in small core–multishell quantum dots by carefully balancing confinement potential and induced lattice strain: the "Goldilocks" effect. *ACS Nano* **10**, 4072 (2016).
4. G.S. Selopal, H. Zhao, Z.M. Wang, F. Rosei. Core/shell quantum dots solar cells. *Adv. Funct. Mater.* **30**, 1908762 (2020).
5. P. Moraitis, R.E.I. Schropp, W.G.J.H.M. Sark. Nanoparticles for luminescent solar concentrators – a review. *Opt. Mater.* **84**, 636 (2018).
6. W. Ma, W. Li, M. Cao, R. Liu, X. Zhao, X. Gong. Large Stokes-shift AIE fluorescent materials for high-performance luminescent solar concentrators. *Org. Electron.* **73**, 226 (2019).
7. C.Y. Lu, J.W. Pan. Quantum-dot single-photon sources for the quantum internet. *Nat. Nanotechnol.* **16**, 1294 (2021).
8. B. Mahler, P. Spinicelli, S. Buil, X. Quelin, J.-P. Hermier, B. Dubertret. Towards non-blinking colloidal quantum dots. *Nat. Mater.* **7**, 659 (2008).
9. F. Purcell-Milton, A.K. Visheratina, V.A. Kuznetsova, A. Ryan, A.O. Orlova, Y.K. Gun'ko. Impact of shell thickness on photoluminescence and optical activity in chiral CdSe/CdS core/shell quantum dots. *ACS Nano* **11**, 9207 (2017).
10. G. Zaiats, D. Yanover, R. Vaxenburg, A. Shapiro, A. Safran, I. Hesseg, A. Sashchiuk, E. Lifshitz. PbSe/CdSe thin-shell colloidal quantum dots. *Z. Phys. Chem.* **229**, 3 (2015).
11. R.Ya. Leshko, I.V. Bilynskyi, O.V. Leshko, M.A. Slusarenko. Electron energy spectrum of the non-concentric spherical core-shell quantum dot. *Micro Nanostruct.* **181**, 207615 (2023).
12. R.Ya. Leshko, O.V. Leshko, I.V. Bilynskyi, V.B. Holskyi. Optical absorption coefficient of non-concentric spherical core-shell quantum dot. *Opt. Commun.* **566**, 130722 (2024).
13. R. Leshko, I. Bilynskyi, O. Leshko, M. Popov, A. Ocheretyanyi. Electron and hole energy spectrum of non-concentric spherical core-shell quantum dot under an externally applied electric field. *Condens. Matter Phys.* **27**, 43703 (2024).
14. R.Ya. Leshko, O.V. Leshko, I.V. Bilynskyi, M.V. Kvyk, Ya.Yu. Melnyk, A.O. Ocheretyanyi, M.Yu. Popov. Electron and hole energy spectra in a non-concentric spherical core-shell quantum dot under a magnetic field. *Phys. Lett. A* **562**, 130996 (2025).
15. R.Ya. Leshko, O.V. Leshko, I.V. Bilynskyi, R.I. Pazyuk. Electron-hole exchange interaction in the non-concentric spherical core-shell quantum dot. *J. Phys. Stud.* **29**, 1701 (2025).
16. J.M. Luttinger, W. Kohn. Motion of electrons and holes in perturbed periodic fields. *Phys. Rev.* **97**, 869 (1955).
17. J.M. Luttinger. Quantum theory of cyclotron resonance in semiconductors: General theory. *Phys. Rev.* **102**, 1030 (1956).
18. A.L. Efros, M. Rosen. Quantum size level structure of narrow-gap semiconductor nanocrystals: Effect of band coupling. *Phys. Rev. B* **58**, 7120 (1998).
19. A. Baldereschi, N.O. Lipari. Spherical model of shallow acceptor states in semiconductors. *Phys. Rev. B* **8**, 2697 (1973).
20. L. Shu-Shen, X. Jian-Bai. Application of plane wave method to the calculation of electronic states of nano-structures. *Chin. Phys. Lett.* **23**, 1896 (2006).
21. S.-S. Li, J.-B. Xia. Binding energy of a hydrogenic donor impurity in a rectangular parallelepiped-shaped quantum dot: Quantum confinement and Stark effects. *J. Appl. Phys.* **101**, 093716 (2007).
22. Al.L. Efros, M. Rosen, M. Kuno, M. Nirmal, D.J. Norris, M. Bawendi. Band-edge exciton in quantum dots of semiconductors with a degenerate valence band: Dark and bright exciton states. *Phys. Rev. B* **54**, 4843 (1996).
23. Y. Liu, S. Bose, W. Fan. Effect of size and shape on electronic and optical properties of CdSe quantum dots. *Optik* **155**, 242 (2018).

24. O. Madelung. *Semiconductors: Data Handbook*, 3rd edition (Springer, 2004) [ISBN: 978-3-540-40488-0].
25. H. Eshet, M. Grünwald, E. Rabani. The electronic structure of CdSe/CdS core/shell seeded nanorods: Type-I or quasi-Type-II? *Nano Lett.* **13**, 5880 (2013).
26. J. Planelles, F. Rajadell, J.I. Climente. Electronic origin of linearly polarized emission in CdSe/CdS dot-in-rod heterostructures. *J. Phys. Chem. C* **120**, 27724 (2016).
27. C. Grivas, C. Li, P. Andreakou, P. Wang, M. Ding, G. Brambilla, L. Manna, P. Lagoudakis. Single-mode tunable laser emission in the single-exciton regime from colloidal nanocrystals. *Nat. Commun.* **4**, 2376 (2013).
28. U.V. Mardolcar, C.A. Nieto de Castro, F.J.V. Santos. Dielectric constant measurements of toluene and benzene. *Fluid Phase Equilib.* **79**, 255 (1992).

Received 02.08.26

Р.Я. Лешко, О.В. Лешко,
І.В. Білинський, Д.С. Карпин

ЕКСИТОННІ СТАНИ У СФЕРИЧНИХ НЕКОНЦЕНТРИЧНИХ КВАНТОВИХ ТОЧКАХ ТИПУ ЯДРО–ОБОЛОНКА

Теоретично досліджено електронну та екситонну структуру неконцентричних сферичних квантових точок типу ядро–оболонка CdSe/CdS, у яких ядро зміщене відносно центра оболонки. Діркові стани обчислено в рамках чотиризонної моделі Латинджера–Кона, розкладеної за базисом плоских хвиль, причому потенціал конфайнменту зі зміщеним ядром враховано безпосередньо, а екситонні стани знайдено методом конфігураційної взаємодії з урахуванням прямої кулонівської взаємодії електрон–дірка та короткодійного обмінного доданка. Зміщення ядра знижує симетрію потенціалу конфайнменту від сферичної до аксіальної та знімає виродження крайового діркового мультиплету, зумовлюючи тонку структуру розщеплення, яка монотонно зростає зі збільшенням зміщення. Той самий механізм перебудовує і екситонний спектр: енергія основного переходу зазнає синього зсуву з наближенням ядра до межі оболонки, тоді як зумовлене обмінною взаємодією розщеплення темного та світлого станів монотонно зростає зі збільшенням зміщення. Розрахований край поглинання кількісно узгоджується з експериментально виміряним значенням. Таке узгодження досягається лише за умови врахування екситонних ефектів, оскільки саме кулонівська взаємодія електрон–дірка забезпечує червоний зсув, необхідний для узгодження теорії з експериментом. Отримані результати вказують на зміщення ядра як на ефективний структурний ступінь свободи для керування як енергією випромінювання, так і тонкою структурою екситона в колоїдних наночастинках типу ядро–оболонка.

Ключові слова: квантова точка ядро–оболонка, неконцентрична наноструктура, CdSe/CdS, тонка структура екситона, розщеплення темного та світлого станів, обмінна взаємодія електрон–дірка, гамільтоніан Латинджера–Кона, метод розкладання за плоскими хвилями.